Electrochemical Reconstruction Engineering: Metal–Organic Gels as Pre-Catalysts for NiOOH/FeOOH Heterostructure to Boost Oxygen Evolution Reaction

Jia-Yang Luo, Yi Yuan, Heng-Yu Ruan, Xue-Qian Wu, Ya-Pan Wu,* Shuang Li, Gaixia Zhang, Shuhui Sun,* and Dong-Sheng Li*

Metal–organic gels (MOG) as new types of soft materials have shown promising applications in various fields such as chemosensors, environmental remediation, and gas adsorption/separation, owing to their high porosity, low density, and high surface area. However, the application of MOG materials in energy electrocatalysis and the active components made from them are rarely perceived. Herein, a new electrochemistry-driven reconstruction strategy to synthesize the NiOOH/FeOOH heterostructure from MOG materials is reported. The reconstructed NiOOH/FeOOH exhibits superior oxygen evolution reaction activity and excellent stability, owing to the synergistic effect of bimetallic centers, the abundant interface between NiOOH and FeOOH, and the plentiful defects. Impressively, the activated Re–FeNi–MOG-4 electrocatalyst displays remarkable catalytic activity with a low overpotential of 220 mV at a current density of 10 mA cm^{-2} and a small Tafel slope of 48 mV dec^{-1} in alkaline electrolyte, outperforming most recently reported electrocatalysts. Herein, a facile and effective electrochemical reconstruction engineering of pre-catalysts is provided and the evolution of self-reconstruction of MOG materials for accelerating the kinetics of the electrocatalytic process is highlighted.

1. Introduction

Splitting water to produce H$_2$ has emerged as an important strategy for converting renewable light or electricity.[1,2] However, the slow kinetic 4e$^-$-transfer oxygen evolution reaction (OER: $4OH^- \rightarrow O_2 + 2H_2O + 4e^-$) at the anode prevents the improvement and enhancement of water decomposition efficiency optimization.[3–5] The key to effective electrocatalyst preparation is to design and reduce overpotential reasonably and accelerate kinetic OER. Although the most mature noble metal oxides, such as RuO$_2$, and IrO$_2$, exhibit remarkable catalytic activity toward the OER, their high cost, scarcity, and corrosion risk limit their practical wide range of applications. Therefore, the exploration of efficient and alternative non-noble metal OER catalysts with high electrocatalytic activity under alkaline conditions is a very attractive frontier topic.[6–10]

Among all non-noble metal catalysts for OER, iron group compounds, such as Fe-, Co-, Ni-based hydroxides, have attracted increasing attention and delivered excellent electrocatalytic properties with lower overpotential and long-term-lasting quality. Particularly, the introduction of exotic metals with strong electronic effects of decoupling control and adjustable active center of electronic structure and conductivity become the main power supply of high OER activity.[11–13] The research on the design, synthesis, structure, and properties regulation of various pure, composite, and different morphologies of iron transition metal hydroxyl oxides has attracted extensive interest from researchers in the fields of chemistry, materials, energy, and environment.[14–17] So far, different synthesis strategies have emerged, such as the direct coprecipitation method, microwave method, electrodeposition method, ultrasonic-assisted synthesis method, and so on.[18–20] However, after the OER reaction process

J.-Y. Luo, Y. Yuan, H.-Y. Ruan, X.-Q. Wu, Y.-P. Wu, S. Li, D.-S. Li
College of Materials and Chemical Engineering
Key Laboratory of Inorganic Nonmetallic Crystalline and Energy
Conversion Materials
China Three Gorges University
Yichang, Hubei 443002, P. R. China
E-mail: wuyapan@ctgu.edu.cn; lidongsheng@ctgu.edu.cn

The ORCID identification number(s) for the author(s) of this article can be found under https://doi.org/10.1002/sstr.202300074.

G. Zhang
Department of Electrical Engineering
École de Technologie Supérieure (ÉTS)
Montréal, Québec H3C 1K3, Canada

Y.-P. Wu, S. Li, D.-S. Li
Hubei Three Gorges Laboratory
Yichang, Hubei 443007, P. R. China

S. Sun
Center Énergie Matériaux Télécommunications
Institut National de La Recherche Scientifique (INRS)
Varennes, Québec J3X 1P7, Canada
E-mail: shuhui.sun@inrs.ca
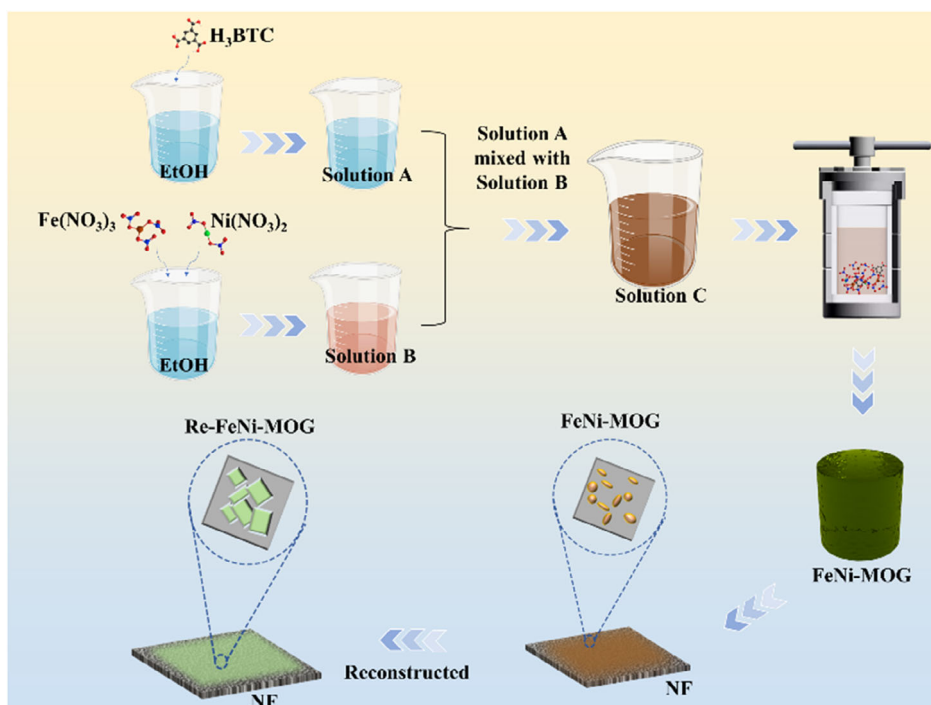
Scheme 1. Schematic illustration of the fabrication of FeNi metal–organic gel (FeNi–MOG) and reconstruction of FeNi-MOG electrocatalysts.
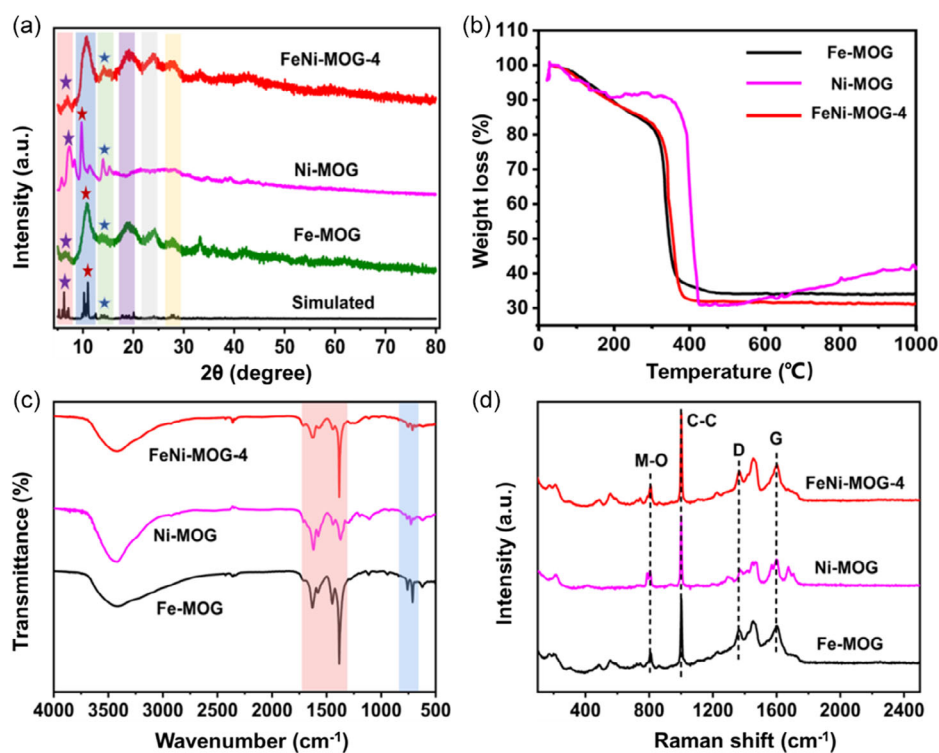

Figure 1. a) PXRD patterns of the as-prepared crystalline MIL-100(Fe) samples, Fe metal–organic gel (Fe–MOG), Ni–MOG, and FeNi–MOG-4. b) Thermogravimetric analysis of Fe–MOG, Ni–MOG, and FeNi–MOG-4. c) Fourier-transform infrared (FTIR) patterns of Fe–MOG, Ni–MOG, and FeNi–MOG-4. d) The ex situ Raman pattern of Fe–MOG, Ni–MOG, and FeNi-MOG-4.

**ADVANCED
SCIENCE NEWS**

www.advancedsciencenews.com

**small
structures**

www.small-structures.com

under strong alkaline conditions, the catalysts often undergo structural transformation or morphology evolution to varying degrees, resulting in changes in the activity of electrocatalytic materials. Therefore, the reasonable application of electrocatalytic reconstruction forging of high-activity OER non-noble metal catalysts has become the key and challenge of the research.[21–25]

In recent years, metal–organic framework (MOF) materials have attracted extensive attention due to their adjustable properties and high specific area. They have proved to be promising templates and precursors for the manufacture of new porous materials. Especially, the structure and composition of MOF materials can be changed after the OER process in alkali conditions, to generate the active hydroxy-oxide or hydroxide compounds. However, understanding the resultant products of different types of MOF reconstruction and the structure–activity relationship is still a great challenge.[26–28] In contrast,

metal–organic gels (MOG) materials, as important variants of MOF materials, are promising candidates to play an important role in an electrocatalytic system. MOG is a new class of soft functional materials that have unique advantages such as easy for high surface area and good compatibility.[29–31] It shows a broad application prospect in gas separation and storage and chemical-sensing detection.[32,33] More studies have demonstrated that the evolution of MOF in the electrocatalytic process of hydroxide-active species can accelerate the conduct of the electrocatalytic reaction. By contrast, the reconstruction of MOG materials in the electrocatalytic process and the elucidation of active species are rarely reported. We believe that the characteristics of MOG materials possess certain advantages in electrocatalytic reconstruction, and it is urgent to start a new journey in the research of electrocatalytic reconstruction and structural performance regulation based on MOG gel materials.
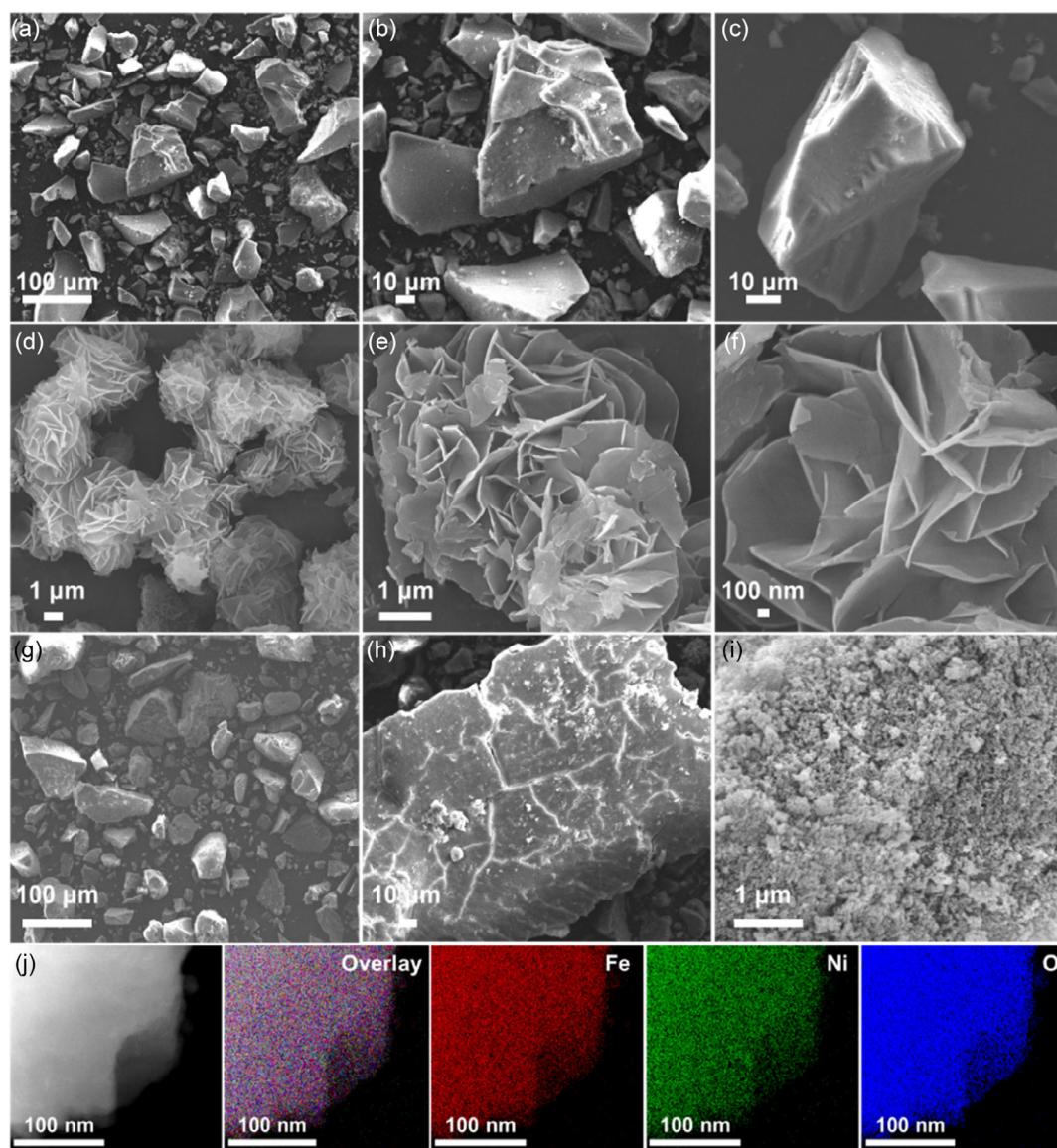

Figure 2. a–c) Scanning electron microscope (SEM) image of Fe–MOG, d–f) SEM image of Ni–MOG, g–i) SEM image of FeNi–MOG-4, and j) scanning transmission electron microscope (STEM) image and EDS elemental mappings of FeNi–MOG-4.

Herein, to realize the MOG-based pre-catalysts of the efficient performance OER with excellent activity and durability, we further designed and synthesized a series of FeNi–MOG materials by one-pot solvothermal method, and characterized the gel pre-catalyst and the heterostructure NiOOH/FeOOH materials after in-situ electrochemical reconstruction, and evaluated the OER properties of the materials before and after reconstruction. Experimental results confirmed that FeNi–MOG-4 and the NiOOH/FeOOH heterojunction with its complete reconstruction showed excellent electrocatalytic OER performance, and the overpotential was as low as 220 mV. This strategy provides a simple method to obtain an effective OER catalyst, and also expands the application of MOGs as pre-catalyst in electrocatalytic OER.

2. Results and Discussion

2.1. Characterization of Morphology and Structure

The synthetic routes of FeNi–MOG and reconstruction of FeNi–MOG electrocatalysts are shown in **Scheme 1**. First, FeNi–MOG gel was synthesized from a mixture of $Fe(NO_3)_3 \cdot 9H_2O$, $Ni(NO_3)_2 \cdot 6H_2O$, and 1,3,5-benzentricarboxylic acid at 160 °C via solvothermal method. Second, the nickel foam electrode loaded with FeNi–MOG material was reconstructed into a three-electrode system. Then, the obtained materials were characterized via powder X-ray diffraction (PXRD), thermogravimetric

(TG), infrared spectroscopy (IR), and ex situ Raman. PXRD analysis was used to explore the crystallinity of FeNi–MOG xerogel, as shown in **Figure 1**a. The PXRD pattern of FeNi–MOG xerogel reveals relatively low crystallinity, as several broad peaks are observed, which is similar to previously reported gels.

In addition, it can be seen that in each position where a peak appears for the MIL-100(Fe) crystal (CCDC:640 536), there exists a corresponding broad peak for the Fe–MOG xerogel, implying that the xerogel materials consist of basic MOF-particle building blocks. Meantime, the TGA profiles of Fe–MOG, Ni–MOG, and FeNi–MOG are shown in Figure 1b, the three materials show similar thermal stabilities. There are two major weight loss processes from 25 to 1000 °C. The first weight loss at 25–200 °C corresponds to solvent evaporation, and the second-stage weight loss may be attributed to the decomposition of organic linkers.

The chemical composition of Fe–MOG, Ni–MOG, and FeNi–MOG xerogel was characterized by Fourier-transform infrared (FTIR) spectrum (Figure 1c) and Raman spectroscopy (Figure 1d). It could be observed that the three samples have similar functional groups. In FTIR spectrum, the two absorption bands at around 1620 and 1425 cm^{-1} are associated with the asymmetric stretch $\nu as(COO)$ and the symmetric stretch mode $\nu sym(COO)$ of carboxylates of H_3BTC. The peak at about 750 cm^{-1} is the vibration of M–O, confirming the successful coordination of the carboxyl group in trimesic acid with the metal.[34] This is further supported by the ex situ Raman spectrum in Figure 1d, which clearly reveals
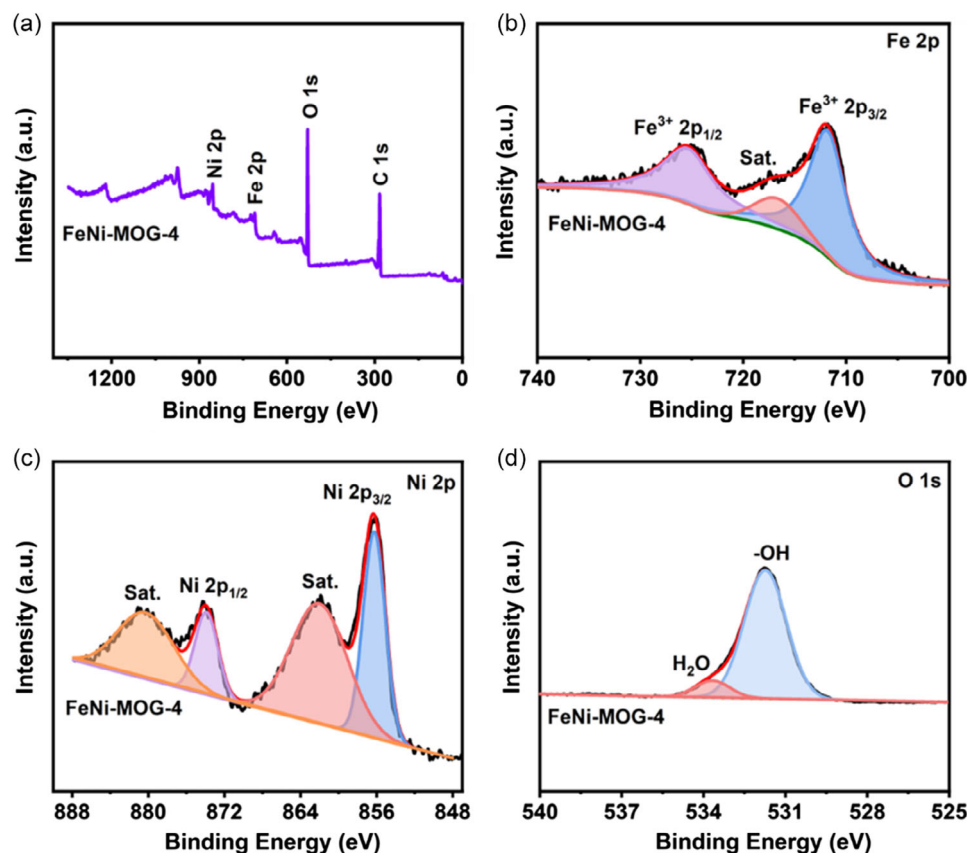

Figure 3. a) X-ray photoelectron spectroscopy (XPS) full survey spectra of FeNi–MOG-4. b) Fe 2*p*, c) Ni 2*p*, and d) O 1*s* of FeNi–MOG-4.

**ADVANCED
SCIENCE NEWS**
www.advancedsciencenews.com

**small
structures**
www.small-structures.com

the M–O vibration (around 800 cm^{-1}) and C–C stretching mode (1000 cm^{-1}) in the fresh sample. The aforementioned basic characterization results indicating that the doped Ni did not change the essential characteristics of the sample.

Meantime, the sample Fe–MOG, Ni–MOG, and FeNi–MOG morphology were revealed by combined scanning electron microscope (SEM) and transmission electron microscope (TEM). SEM images show that the Fe–MOG exhibits an irregular block structure that is composed of different particle sizes. The Ni–MOG shows the morphology of flake petals. After doping Ni, the overall morphology of the sample presents a blocky structure, but the size of the blocky particles decreases. Subsequently, the corresponding high-angle annular dark-field imaging (HAADF) and energy dispersive X-ray spectroscopy (EDS) mappings in **Figure 2**j confirmed that the Ni atoms are uniformly distributed in Fe–MOG.

The surface compositions and electronic states of the FeNi–MOG-4 sample were characterized through X-ray photoelectron spectroscopy (XPS) (**Figure 3**). As shown in Figure 3a, the survey XPS spectrum demonstrated that the sample consists of Fe, Ni, O, and C elements. The high-resolution core spectrum of Fe 2p is presented in Figure 3b. Two peaks at binding energies (BEs) around 711.8 and 725.7 eV are consistent with the characteristic peaks of Fe2$p_{3/2}$ and Fe 2$p_{1/2}$. As for the Ni 2p spectrum, two peaks at BEs around 856.5 and 874.4 eV are consistent with the characteristic peaks of Ni 2$p_{3/2}$ and Ni 2$p_{1/2}$, accompanied by two prominent shake-up satellite peaks, which are attributed to the Ni^{2+} ions in FeNi–MOG-4. The O 1s XPS spectra were fitted into four components located at 531.7 and 533.7 eV, corresponding to the surface hydroxyl group and adsorbed water molecules, respectively.

To further assess the self-reconstruction of the optimized catalyst in the test environment, a series of characterizations were assessed. The formation electrochemical reconstruction process of Re–FeNi–MOG-4 is schematically illustrated in **Figure 4**a. The PXRD analysis indicates that the Re–FeNi–MOG-4 is composed of NiOOH and FeOOH phases (Figure 4b), suggesting that the FeNi–MOG restructures under electric conditions. In addition, FTIR (Figure 4c) indicated that absorption bands at 1623, 1382, and 820 cm^{-1} were assigned to the symmetrical stretching vibration of C=C, C=O, and C–C of FeNi–MOG. After electrochemical reconstruction, these characteristic peaks were not observed in Re–FeNi–MOG-4. Meantime, the reconstructed samples generated from other MOGs such as Re–Fe–MOG, Re–FeNi–MOG-1, Re–FeNi–MOG-2, Re–FeNi–MOG-3, and Re–FeNi–MOG-5 have been prepared under the similar strategy and characterized by X-ray diffraction (XRD) and IR techniques (Figure S10, Supporting Information). The XRD main peaks and the IR characteristic peaks of the five reconstructed samples are uniformly consistent with pure Re–Fe–MOG, which indicates that the different amounts of nickel did not affect the structure of the product after the reconstruction process. As a real active species, FeNi–MOG will participate in the formation of active intermediates in the OER reaction, thus accelerating the whole reaction process. The inductively
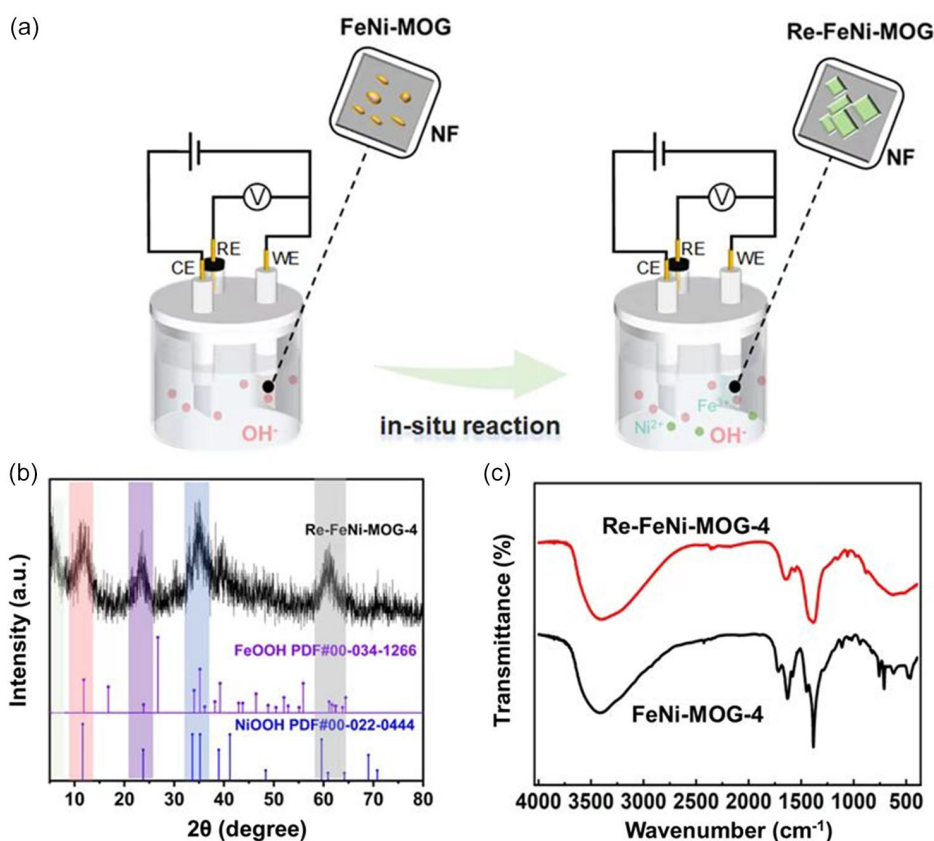

Figure 4. a) Sketch of the electrochemical in situ reconstruction of FeNi–MOG-4. b) PXRD patterns of the thorough reconstruction of FeNi–MOG into NiOOH/FeOOH heterostructure, and c) IR of FeNi–MOG, and Re–FeNi–MOG-4.

coupled plasma atomic emission spectrometry (ICP-AES) measurements for FeNi–MOG-4 suggested that the molar ratio of Fe^{3+}:Ni^{2+} in the precatalyst stage is $\approx$3:4 (Table S1, Supporting Information).

To further clarify the chemical structure of the Re–FeNi–MOG-4, the detailed morphology structure of Re–FeNi–MOG-4 after self-reconstruction was characterized by SEM and TEM (**Figure 5**). Further, the high-resolution TEM (HRTEM) image of the nanosheet (Figure 5d–g) displays two distinct lattice fringes with d-spacing of 0.836 and 1.095 nm (Figure 5e,f), corresponding to the (105) plane of NiOOH and the (031) plane of FeOOH, respectively. The HAADF-STEM image and the corresponding EDS mapping shown in Figure 5h demonstrated that Fe, Ni, and O elements were uniformly dispersed in the nanosheet, but C was not nearly observed after self-reconstruction.

In addition, to elucidate the influences of Ni-doping and the corresponding effect on the surface chemical properties and the chemical state of Re–FeNi–MOG-4, XPS was performed. All XPS spectra are demarcated with C1s at around 284.8 eV as the standard. As shown in **Figure 6**a, the survey spectrum shows the presence of Fe, Ni, C, and O elements in all samples. The high-resolution Fe 2p spectrum of Re–NiFe–MOG-4 (Figure 6b) could be deconvoluted into two valence states of Fe species including Fe^{2+} $2p_{3/2}$ (705.7 eV) and Fe^{3+} $2p_{3/2}$ (725.2 eV),

revealing the coexistence of Fe^{3+} and surface reduced Fe^{2+} in Re–NiFe–MOG. The Fe^{3+} peak of Re–FeNi–MOG-4 is shifted by 0.3 eV compared to FeNi–MOG-4, demonstrating strong electronic interaction between Fe and Ni metals. As shown in Figure 6c, two distinct characteristic peaks at positions 856.5 and 874.2 eV belong to Ni $2p_{3/2}$ and Ni $2p_{1/2}$, respectively, and are accompanied by their respective satellite peaks at positions 862.4 and 880.6 eV, respectively. In particular, the peak at 858.9 eV indicates the appearance of the Ni^{3+} oxidation state, which was attributed to the crystal and amorphous interface formed by the interaction between Ni ion and OH^-. Compared with pure FeNi–MOG-4, the BE position shifts to the positive direction (0.73 eV), indicating that oxidation state is increased by the loss of more electrons under the regulation of cation. Meanwhile, the O 1s XPS spectrum of Re–FeNi–MOG-4 exhibits more content of metal–O bonds, further confirming that more oxyhydroxides are formed in Re–FeNi–MOG-4 (Figure 6d). The electronic environment modulated by the introduction of cations into FeNi–MOG-4 favors the formation of metal high-valence active species in Re–FeNi–MOG-4-based electrocatalysts.

2.2. Electrocatalytic Performance Evaluation

The OER performance of Fe–MOG, Ni–MOG, FeNi–MOG-4, and Re–FeNi–MOG-4 as electrochemical catalysts were first
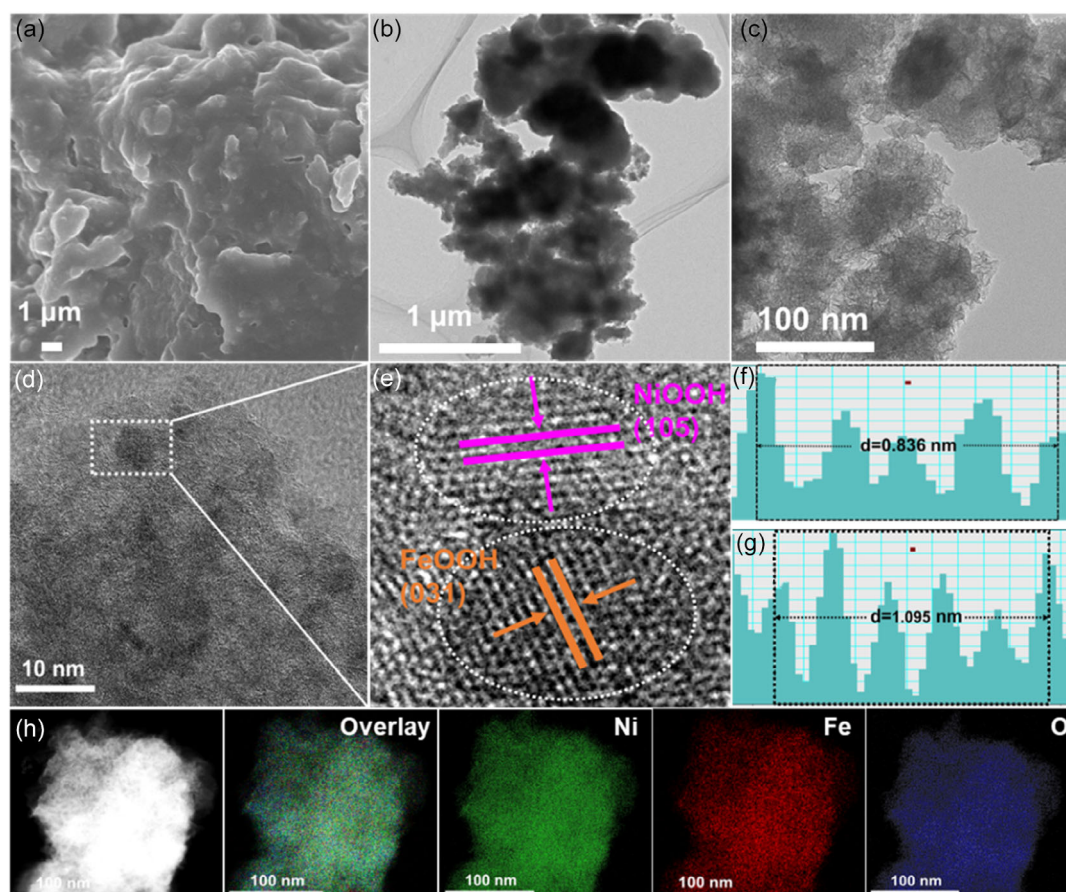

Figure 5. Morphological characterizations of Re–FeNi–MOG-4. a) SEM image of Re–FeNi–MOG-4. b,c) Transmission electron microscope (TEM) images with different magnifications. d,e) High-resolution TEM (HRTEM) images. g,f) The interplanar spacings of the lattice fringes. h) STEM image and corresponding elemental mapping images of Re–FeNi–MOG-4.
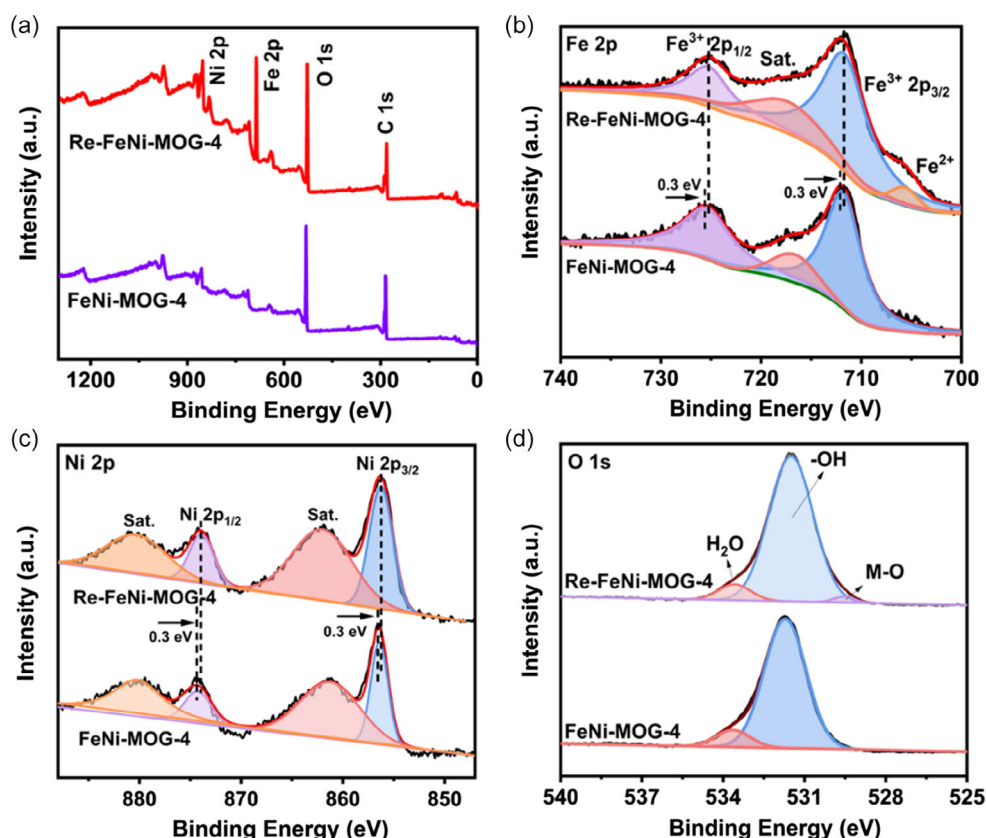
ADVANCED
SCIENCE NEWS
www.advancedsciencenews.com

small
structures
www.small-structures.com

Figure 6. a) XPS full survey spectra of FeNi–MOG-4 and Re–FeNi–MOG-4. The high-resolution XPS spectra of b) Fe 2p, c) Ni 2p, d) O 1s of FeNi-MOG-4, and Re-FeNi-MOG-4.

studied in 1.0 M KOH alkaline electrolyte at room temperature. For comparison, the precursors FeNi–MOG-4 and IrO$_2$ were also measured as working electrodes. All of the electrochemical measurements are carried out with a typical three-electrode system in a 1.0 M KOH aqueous solution, and the potential values are calibrated against the reversible hydrogen electrode (RHE). **Figure 7**a shows the typical linear-sweep voltammetry (LSV) curve of Re–FeNi–MOG-4, along with those of Fe–MOG, Ni–MOG, FeNi–MOG-4, and IrO$_2$ as references. The Re–FeNi–MOG-4 electrode only needs a small overpotential of 220 mV to drive the water oxidation reaction at 10 mA cm^{-2}, which is smaller than Fe–MOG (479 mV), Ni–MOG (300 mV), and FeNi–MOG-4 (270 mV), which is significantly better than commercial IrO$_2$ (340 mV) (Figure 7b). It is noted that the Re–FeNi–MOG-4 sample shows superior OER activity to the other reported advanced catalysts (Table S1, Supporting Information). In addition, the Tafel slope is another crucial index for assessing the kinetic activity of OER in the electrochemical process. Re–FeNi–MOG-4 has the smallest Tafel plot (48 mV dec^{-1}) compared with pure Fe–MOG (137 mV dec^{-1}), Ni–MOG (125 mV dec^{-1}), FeNi–MOG-4 (61 mV dec^{-1}), and IrO$_2$ (130 mV dec^{-1}), indicating fast surface kinetics (Figure 7b). Further, electrochemical surface area was obtained at different scan rates from 20 to 100 V versus RHE to estimate double-layer capacitance (Cdl). As expected, the Re–FeNi–MOG-4 sample has a Cdl value of 299 mF cm^{-2}, which is higher than that of Fe–MOG (80 mF cm^{-2}) and FeNi–MOG-4

(261 mF cm^{-2}), indicating that Re–FeNi–MOG-4 has a large electrochemically active surface area (Figure 7c). This might be due to the relatively high surface area and porous structure. In addition, the η_{10} value and Tafel slope of Re–FeNi–MOG-4 are also much lower than other OER catalysts recently reported in alkaline media (Figure 7d and Table S2, Supporting Information). Meantime, the turnover frequency (TOF) was calculated to study the intrinsic activity of the OER electrocatalysts, as shown in Figure S13, Supporting Information, and the Re–FeNi–MOG-4 shows a much higher TOF value of 0.5390 s^{-1} than those of other MOG materials at the given potential of 220 mV (Fe–MOG for 0.0199 s^{-1}, Ni–MOG for 0.0202 s^{-1}, and FeNi–MOG-4 for 0.0264 s^{-1}). Moreover, the TOF values of Re–FeNi–MOG-4 are higher than single-metal MOG, further revealing the better OER performances of electrocatalysts constructed from bimetal MOG.

The electrode kinetics of the catalysts were further investigated using electrochemical impedance spectroscopy (EIS). Nyquist plots (**Figure 8**a) further indicate that Re–FeNi–MOG-4 displays the smallest charge-transfer resistance (15.5 Ω), which is much lower than that of FeNi–MOG-4 (29.2 Ω). This indicates that the Re–FeNi–MOG-4 possesses a faster electron transfer rate and better conductivity, which is beneficial for the OER process. Furthermore, stability is another important parameter for evaluating an electrocatalyst's performance. As a result, a long-term chronoamperometry test was performed to assess the durability in a 1.0 M KOH solution. As presented in Figure 8b, the current
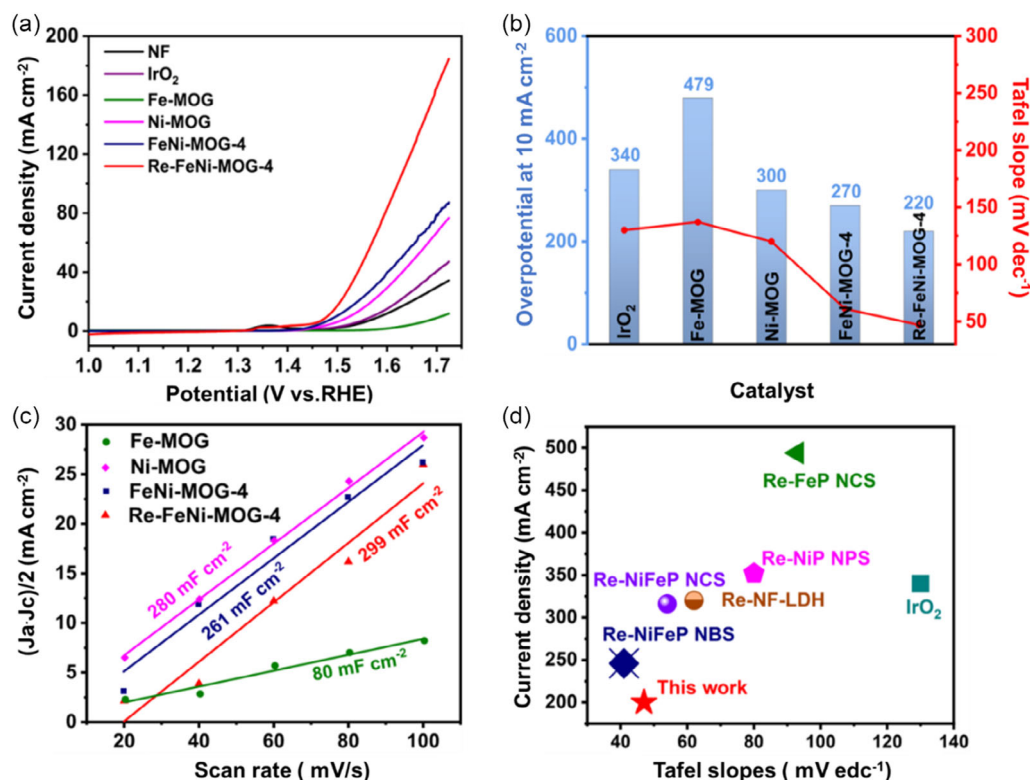
Figure 7. Oxygen evolution reaction (OER) performance of the as-prepared electrodes. a) linear-sweep voltammetry (LSV) plots of different electrocatalysts. b) Comparison of overpotential and Tafel slope of electrocatalysts. c) Double-layer capacitance is determined by the CV curves. d) Comparison of overpotential and Tafel slope of Re–FeNi–MOG-4 with recently reported reconstructed catalysts.
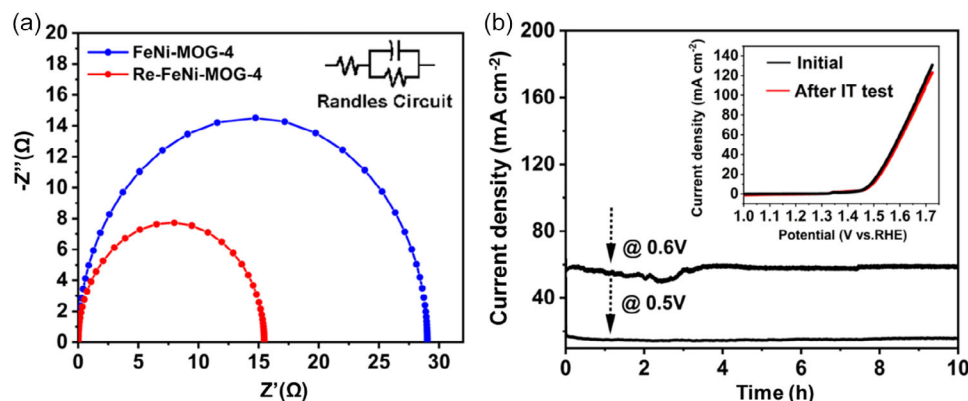

Figure 8. a) Nyquist plots of different catalysts. b) Chronopotentiometry curve of OER for Re–FeNi–MOG-4 at the current density of 10 and 60 mA cm^{-2}, respectively. The inset in (b) shows the LSV curves for Re–FeNi–MOG-4 (black) and LSV curve (red) after the 10 h test.

density almost keeps unchanged at an overpotential of 0.5 and 0.6 V for 10 h. After the stability test, the LSV curve was basically coincident with the curve before the test which shows that the material has good stability. In addition, the electrocatalytic OER activities of the reconstructed series of samples were also carefully evaluated (Figures S10–S12, Supporting Information), it can be observed that the performance of the reconstructed sample has been greatly improved compared with that of the corresponding gel material, further confirming that the reconstruction

strategy is helpful to improve the oxygen evolution performance of the materials. Some additional characterizations such as XRD, SEM, and TEM techniques were performed to assess the stability of Re–FeNi–MOG-4 after OER. As can be seen, the XRD patterns of the collected samples after the OER still exhibited unchanged phase characteristics compared with the original FeNi–MOG-4 structure (Figure S14, Supporting Information). The morphology of the Re–FeNi–MOG-4 after the OER test (Figure S15a–c, Supporting Information) indicates that the irregular block

feature of FeNi–MOG-4 is inherited. The HRTEM analysis (Figure S15d–g, Supporting Information) exhibits clear lattice fringes, which could be assigned to (105) planes of the NiOOH and (031) planes of FeOOH. These results suggest that Re–FeNi–MOG-4 maintains the original structural stability after the OER process.

3. Conclusion

To summarize, we presented an electrochemical in situ strategy to synthesize the NiOOH/FeOOH heterostructural material generated from the FeNi–MOG precatalyst for OER. During the OER process, irreversible deep self-reconstruction of FeNi–MOG resulted in the formation of NiOOH/FeOOH. Due to the porous structure of MOG and the synergistic coupling between Fe and Ni hydroxyl oxide particles generated by in situ electrochemical reconstruction, the as-obtained Re–FeNi–MOG-4 demonstrates outstanding OER performance with a low overpotential and excellent durability. We believe that this strategy can help design superior OER electrocatalysts, providing a promising approach for developing durable electrochemical catalysts and also enriching the research scope of MOG-derived materials and contributing to the exploration of more efficient electrocatalysts.

4. Experimental Section

Chemical Reagents: Nickel nitrate hexahydrate (Ni(NO$_3$)$_2$·6H$_2$O), ferric nitrate nonahydrate (Fe (NO$_3$)$_2$·9H$_2$O), ethanol (CH$_3$CH$_2$OH), deionized water (H$_2$O), and potassium hydroxide (KOH) were purchased from Sinopharm Chemical Reagent Co. Ltd. Nafion solution (5 wt%) was purchased from Macklin Chemical Reagent. All purchased chemicals were not further purified and all solvents were analytical grade.

Preparation of Fe–MOG: In detail, 1.0 mmol H$_3$BTC and 1.5 mmol Fe(NO$_3$)$_3$·9H$_2$O were separately dissolved in 5 mL CH$_3$CH$_2$OH, and then the two solutions were quickly mixed. Afterward, the resulting homogeneous mixture was maintained at 160 °C for 5 h in a closed container. After cooling to room temperature, a light brown gel was collected, thoroughly washed with deionized water several times, and then dried at 80 °C for 12 h under vacuum.

Preparation of FeNi-MOG with Different Ni/Fe Ratios: In a typical synthesis, 1.0 mmol H$_3$BTC, 0.65 mmol Fe(NO$_3$)$_3$·9H$_2$O, and 0.85 mmol Ni(NO$_3$)$_2$·6H$_2$O were separately dissolved in 5 mL of CH$_3$CH$_2$OH, and the two solutions were rapidly mixed. The resulting homogeneous solution was then maintained at 160 °C for 3 h in a closed container. After cooling to room temperature, the green gel was formed. FeNi–MOG-1, FeNi–MOG-2, FeNi–MOG-3, and FeNi–MOG-5 gels were synthesized in a similar way to that for the FeNi-MOG-4 gel, except that Fe (NO$_3$)$_3$·9H$_2$O (0.65 mmol) and Ni(NO$_3$)$_2$·6H$_2$O (0.85 mmol) was replaced by Fe(NO$_3$)$_3$·9H$_2$O (1.13 mmol) and Ni(NO$_3$)$_2$·6H$_2$O (0.37 mmol), Fe(NO$_3$)$_3$·9H$_2$O (0.90 mmol) and Ni(NO$_3$)$_2$·6 H$_2$O (0.60 mmol), Fe(NO$_3$)$_3$·9H$_2$O (0.75 mmol) and Ni(NO$_3$)$_2$·6H$_2$O (0.75 mmol), and Fe(NO$_3$)$_3$·9H$_2$O (0.56 mmol) and Ni(NO$_3$)$_2$·6H$_2$O (0.94 mmol), respectively.

In Situ Electrochemical Activation for Preparing Re–FeNi–MOG-4: The in situ electrochemical activations were carried out in 1.0 KOH under an N$_2$ atmosphere to avoid possible oxidation caused by O$_2$ in air. The as-prepared working electrode FeNi–MOG–4 pre-catalyst was directly used as an OER catalyst which tabled on the nickel foam and immersed in 1.0 KOH, cyclic voltammetry (CV) activation was conducted at 0.6–0.8 V versus RHE, resulting material reconstruction, entitled as Re–FeNi–MOG.

Characterization: XRD patterns were obtained on a Rigaku Ultima IV diffractometer (Cu Kα radiation, $\lambda = 1.5406$ Å, the 2θ range of 5°–80°). FTIR spectra (KBr pellets) were conducted on a Thermo Electron NEXUS 670 FTIR spectrometer. The morphologies and microstructures were investigated using a field-emission SEM (JEOLJSM-6700F) and a TEM (JEOLJEM-2010F). TG curves were gained on a Netzsch model 449C thermal analyzer heated from 25 to 1000 °C with a heating rate of 10 °C min^{-1} under an air atmosphere. XPS data were obtained using an ESCALAB 250 with a monochromatic Al Kα X-ray source, and C 1s was used to calibrate the BEs to 284.8 eV.

Electrochemical Measurements: Typically, the obtained samples were ground into a powder and then added to a 1.0 mL centrifugal tube with a mixed solution of 0.6 mL of H$_2$O, 0.3 mL of EtOH, and 0.1 mL of Nafion. Then, the ink was subsequently sonicated to ensure well-distributed dispersion. Then, the ink was drop-cast onto prepared electrodes. All electrochemical measurements were tested at 25 °C on a CHI 660e electrochemical workstation. In general, OER measurements were carried out in a three-electrode electrochemical cell. Before the electrochemical tests, the electrolyte (1.0 M KOH) was degassed by bubbling oxygen for 30 min. A glassy carbon disc electrode (Ø = 3 mm) electrode modified with the catalysts mentioned before was used as the working electrode. A Pt wire electrode was chosen as the counter electrode. The Hg/HgO electrode was used as the reference electrode, and the potential was converted to the RHE via the Nernst equation: $E_{RHE} = E_{Hg/HgO} + 0.098$ V $+ 0.059$ pH. LSV and CV were recorded with a scan rate of 5 mV s^{-1}. Tafel plots were derived from the LSV curves. EIS was carried out at 1.6 V versus RHE with a frequency range from 0.01 Hz to 1000 kHz. The current–time (I–T) curves were tested at the overpotential corresponding to the current density of 10 mA cm^{-2}. All of the electrochemical data were offered without iR correction.

Supporting Information

Supporting Information is available from the Wiley Online Library or from the author.

Conflict of Interest

The authors declare no conflict of interest.

Data Availability Statement

The data that support the findings of this study are available from the corresponding author upon reasonable request.

[1] G. Zhang, Z. Li, J. Zeng, L. Yu, C. Zuo, P. Wen, Y. Liu, L. Zhong, H. Chen, Y. Qiu, *Appl. Catal., B.* **2022**, *319*, 121921.

[2] F. Zeng, C. Mebrahtu, L. Liao, A. K. Beine, R. Palkovits, *J. Energy Chem.* **2022**, *69*, 301.

[3] M. Chen, H. Li, C. Wu, Y. Liang, J. Qi, J. Li, E. Shangguan, W. Zhang, R. Cao, *Adv. Funct. Mater.* **2022**, *32*, 2206407.

[4] W. Xie, J. Huang, L. Huang, S. Geng, S. Song, P. Tsiakaras, Y. Wang, *Appl. Catal. B* **2022**, *303*, 120871.

[5] X. Zhang, H. Zhao, C. Li, S. Li, K. Liu, L. Wang, *Appl. Catal., B* **2021**, *299*, 120641.

[6] S. Chen, C. Yu, Z. Cao, X. Huang, S. Wang, H. Zhong, *Int. J. Hydrogen Energy.* **2021**, *46*, 7037.

[7] A. Dutta, N. Pradhan, *J. Phys. Chem. Lett.* **2017**, *8*, 144.

[8] C. Guo, J. Liu, F. Quan, S. Zhang, T. Yu, Y. Mo, R. Guo, X. Liu, Y. Liu, W. Mu, X. Lei, *J. Alloys Compd.* **2022**, *920*, 165898.

[9] Y. Wu, C. Sun, H. Wang, S. Ji, B. G. Pollet, J. Lu, X. Tian, H. Liang, X. Wang, R. Wang, *J. Alloys Compd.* **2022**, *903*, 163855.

[10] C. Zhou, E. Hu, S. Liu, W. Cao, Y. Zhu, H. Zhang, T. Zhu, X. Gao, Z. Lin, *J. Colloid Interface Sci.* **2022**, *622*, 319.

[11] W. Hua, H. Sun, M. Jiang, L. Ren, Y. Zhang, J. G. Wang, *J. Mater. Chem. A.* **2022**, *10*, 7366.

[12] T. Jiang, W. Xie, S. Geng, R. Li, S. Song, Y. Wang, *Chin. J. Catal.* **2022**, *43*, 2434.

[13] Y. Zhu, K. Yue, C. Xia, S. Zaman, H. Yang, X. Wang, Y. Yan, B. Y. Xia, *Nanomicro Lett.* **2021**, *13*, 137.

[14] J. Kim, Y. Choi, D. K. Lim, J. Yoo, H. G. Seo, S. Kim, S. Kim, W. Jung, *J. Mater. Chem. A* **2022**.*10*, 20886

[15] J. Liu, P. Ding, Z. Zhu, W. Du, X. Xu, J. Hu, Y. Zhou, H. Zeng, *Small* **2021**, *17*, 2101671.

[16] X. Liu, R. Guo, K. Ni, F. Xia, C. Niu, B. Wen, J. Meng, P. Wu, J. Wu, X. Wu, L. Mai, *Adv. Mater.* **2020**, *32*, 2001136

[17] X. Liu, J. Meng, K. Ni, R. Guo, F. Xia, J. Xie, X. Li, B. Wen, P. Wu, M. Li, J. Wu, X. Wu, L. Mai, D. Zhao, *Cell Rep. Phys. Sci.* **2020**, *1*, 100241.

[18] X. Liu, J. Meng, J. Zhu, M. Huang, B. Wen, R. Guo, L. Mai, *Adv. Mater.* **2021**, *33*, 2007344.

[19] X. Liu, F. Xia, R. Guo, M. Huang, J. Meng, J. Wu, L. Mai, *Adv. Funct. Mater.* **2021**, *31*, 2101792.

[20] X. Feng, Y. Xiao, H. H. Huang, Q. Wang, J. Wu, Z. Ke, Y. Tong, J. Zhang, *Chem. Asian J.* **2021**, *16*, 3213.

[21] W. Luo, Y. Wang, L. Luo, S. Gong, M. Wei, Y. Li, X. Gan, Y. Zhao, Z. Zhu, Z. Li, *ACS Catal.* **2022**, *12*, 1167.

[22] P. Lyu, P. Nachtigall, *Catal. Today* **2020**, *345*, 220.

[23] A. Mondal, S. Ganguli, H. R. Inta, V. Mahalingam, *ACS Appl. Energy Mater.* **2021**, *4*, 5381.

[24] S. H. Talib, Z. Lu, X. Yu, K. Ahmad, B. Bashir, Z. Yang, J. Li, *ACS Catal.* **2021**, *11*, 8929.

[25] K. Wang, Y. Li, J. Hu, Z. Lu, J. Xie, A. Hao, Y. Cao, *Chem. Eng. J.* **2022**, *447*, 137540.

[26] S. Wang, Q. Li, S. Sun, K. Ge, Y. Zhao, K. Yang, Z. Zhang, J. Cao, J. Lu, Y. Yang, Y. Zhang, M. Pan, Z. Lin, L. Zhu, *J. Mater. Chem. A* **2022**, *10*, 5350.

[27] X. Wei, S. Cao, H. Xu, C. Jiang, Z. Wang, Y. Ouyang, X. Lu, F. Dai, D. Sun, *ACS Mater. Lett.* **2022**, *4*, 1991.

[28] D. Yao, C. Tang, A. Vasileff, X. Zhi, Y. Jiao, S. Z. Qiao, *Angew. Chem., Int. Ed. Engl.* **2021**, *60*, 18178.

[29] P. Sutar, T. K. Maji, *Chem. Commun.* **2016**, *52*, 8055.

[30] A. K. Chaudhari, J. C. Tan, *Chem. Commun.* **2017**, *53*, 8502.

[31] D. Ghosh, M. Gorecki, G. Pescitelli, K. K. Damodaran, *Angew. Chem. Int. Ed. Engl.* **2021**, *60*, 24406.

[32] Y. H. Shih, J. H. Chen, Y. Lin, H. T. Chen, C. H. Lin, H. Y. Huang, *Chem. Commun.* **2017**, *53*, 5725.

[33] Y. Xiao, Q. Wang, X. Feng, J. Wu, P. Liao, Y. Tong, J. Zhang, *J. Mater. Chem. A* **2021**, *9*, 17451.

[34] L. Yaqoob, T. Noor, N. Iqbal, H. Nasir, N. Zaman, *Catalysts* **2019**, *9*, 856.